# Microwave spectroscopy reveals the quantum geometric tensor of topological Josephson matter

R. L. Klees,[1] G. Rastelli,[1,2] J. C. Cuevas,[3] and W. Belzig[1]

[1]*Fachbereich Physik, Universität Konstanz, D-78457 Konstanz, Germany*
[2]*Zukunftskolleg, Universität Konstanz, D-78457, Konstanz, Germany*
[3]*Departamento de Física Teórica de la Materia Condensada and Condensed Matter Physics Center (IFIMAC), Universidad Autónoma de Madrid, E-28049 Madrid, Spain*

(Dated: October 29, 2018)

Topology is providing new insight into condensed matter physics problems. Concepts like Chern numbers and their relation to physical phenomena have become very familiar, but actually, key quantities like the quantum geometric tensor, which provides a much deeper information about quantum states, remain experimentally difficult to access. Recently it has been shown that multi-terminal superconducting junctions constitute an ideal playground to mimic topological systems in a controlled manner. Here, we theoretically study the spectrum of Andreev bound states in topological Josephson matter and demonstrate that the full information of the quantum geometric tensor of the ground state manifold can be extracted with the help of microwave spectroscopy. In particular, we develop the concept of artificially polarized microwaves, which can be used to obtain both the quantum metric tensor and the Berry curvature. The quantized integrated absorption provides a direct evidence of topological quantum properties of the Andreev states.

## I. INTRODUCTION

Presently there is a huge interest in condensed matter physics in topologically nontrivial systems and in the last two decades, there has been a great effort to find novel types of topological quantum matter. A famous example is that of topological insulators[1,2], which have symmetry-protected, conducting edge-states while the bulk is insulating. Another key case is that of topological semimetals, materials in which the valence and the conduction bands touch at isolated points in the bulk. Two basic examples are the so-called Dirac and Weyl semimetals, whose low-energy properties can be described with Dirac or Weyl Hamiltonians, respectively, in the vicinity of those isolated points[3]. In the case of Weyl semimetals, such singularities are referred to as "diabolic" points and play an important role in the topological characterization of the band structure as they constitute monopoles of the Berry flux[4]. Another class of topological materials are topological superconductors in which one can create Bogoliubov quasiparticles at zero energy, the so-called Majorana zero modes, which could be potentially used in a novel kind of topologically protected quantum computation due to their non-Abelian braiding statistics[5]. All these cases are now being investigated in the novel research line known as topological band theory[6].

On the other hand, the idea of quantum computation based on the Andreev bound states (ABS) appearing in superconducting weak links, also known as Josephson junctions, has also been around for quite some time[7,8]. In this case, there is no need for exotic topological materials and the ABS can be easily tuned when the junctions are embedded in rf-SQUIDs (superconducting quantum interference devices). Moreover, ABS can be experimentally accessed and coherently manipulated by microwave spectroscopy[9–11] and supercurrent spectroscopy[12]. Very recently, multiterminal Josephson junctions made of conventional superconductors have been predicted to exhibit nontrivial topology in the space of superconducting phases for four[13–17] and three[18–21] leads, in analogy to nontrivial topology in momentum space for topological materials. Moreover, it has been shown that the quantized transconductance across two terminals in such topological Josephson matter is a manifestation of the Chern number, an integer-valued topological number, of the occupied ABS[13,16,17]. Although it is challenging to fabricate multiterminal Josephson junctions and control its superconducting phases[22], a realization of a 3-terminal superconducting junction in a double-SQUID configuration and the investigation of its topological properties has already been reported[23].

Since the nontrivial Chern number follows from an integration of the Berry curvature over periodic parameters, accessing the more fundamental geometrical properties contained in the so-called quantum geometric tensor provides additional information about the geometry of the state space manifolds[24]. The quantum geometric tensor can be decomposed into a symmetric part, the metric (Fubini-Study metric), which measures the "distance" between two adiabatically connected states and an antisymmetric part, the Berry curvature, which contains information about the geometrical phase acquired by an adiabatic change of parameters. There have been several proposals about how to measure the elements of the quantum metric experimentally, e.g., via the noise spectral function[25,26], but it has also been shown that in general the quantum metric can be obtained through periodic driving of the space-defining parameters[27]. Moreover, another proposal showed that the response of circular shaking of a system reveals the momentum space Berry curvature and its integrated Chern number[28,29]. In addition, experiments measuring Berry curvatures and the resulting nontrivial Chern numbers have already been successfully carried out in ultracold fermionic atoms[30,31], superconducting qutrits[32] and coupled fiber loops[33].

In this work, we present a way to experimentally access the full quantum geometric tensor of the ground state manifold of the low-energy ABS in multiterminal Josephson junctions. Inspired by the method of periodically driving different parameters, we shall introduce the concept of artificially linearly or circularly polarized microwave absorption spectroscopy for the case of superconducting multiterminal junctions. Figure 1 schematically summarizes the general procedure for the specific example of a 4-terminal Josephson junction. In the following, we shall show how this type of spectroscopy can be used to extract the full information of the Fubini-Study metric tensor and the Berry curvature in these multiterminal Josephson junctions. We anticipate that this approach can be used in a large variety of topological Josephson matter and it can provide a novel insight into the nature of quantum states in these systems.

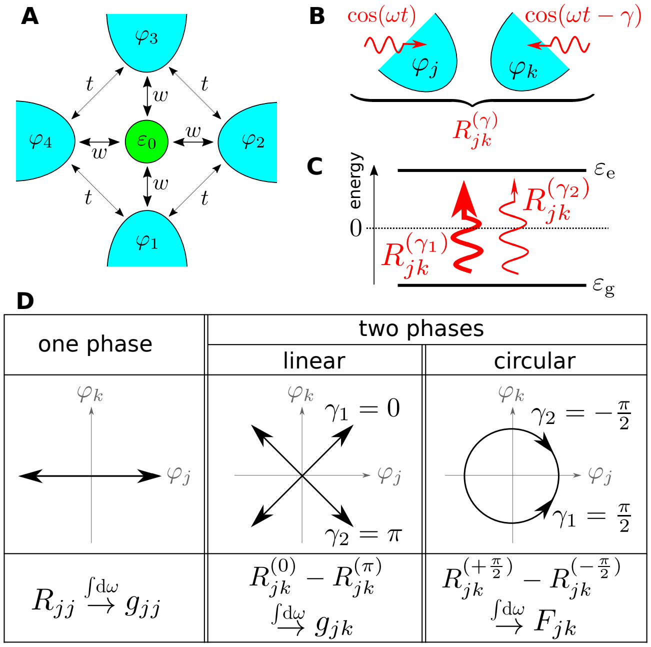

Figure 1. *Application of polarized microwave spectroscopy in multiterminal junctions.* **(A)** Microscopic model of the 4-terminal Josephson junction. Four superconducting leads, each with a pairing phase $\varphi_j$ $(j = 1, 2, 3, 4)$, are connected to a normal quantum dot with level $\varepsilon_0$ via the couplings $w$ and leads are directly connected to each other by the couplings $t \ll w$. **(B)** A periodic modulation of two phases $\varphi_j$ and $\varphi_k$ $(j \neq k)$ at frequency $\omega$ leads to transitions with rates of absorption $R_{jk}^{(\gamma)}$, where $\gamma$ is the relative phase between the two drivings. **(C)** Two measurements with different relative phases $\gamma_1 \neq \gamma_2$ lead to different transition rates $R_{jk}^{(\gamma_1)} \neq R_{jk}^{(\gamma_2)}$ between the ground state at energy $\varepsilon_{\mathrm{g}}$ and the excited state at energy $\varepsilon_{\mathrm{e}}$. **(D)** Schema of how to extract the elements of the quantum geometric tensor $\chi_{jk} = g_{jk} - iF_{jk}/2$, where $g_{jk}$ is the metric tensor and $F_{jk}$ is the Berry curvature. Driving of one phase $\varphi_j$ allows for the detection of the diagonal elements $g_{jj}$, while linear (circular) driving of two phases $\varphi_j$ and $\varphi_k$ $(j \neq k)$ allows for the extraction of the off-diagonal elements $g_{jk}$ $(F_{jk})$.

## II. RESULTS

### A. Model and the effective Hamitonian on the dot

Our goal is to study the microwave spectroscopy of topologically nontrivial ABS in superconducting multiterminal junctions. For the sake of concreteness, we first consider the particular realization that is schematically represented in Figure 1A. In this system, four superconducting (SC) terminals are connected to a normal conducting region that consists of a single level, noninteracting quantum dot. In the absence of microwave drive, the Hamiltonian of this system reads

$$H = H_{\mathrm{D}} + \sum_{j=1}^{4}\left(H_{\mathrm{S}}^{(j)} + H_{\mathrm{S-D}}^{(j)} + H_{\mathrm{S-S}}^{(j,j+1)}\right). \qquad (1)$$

Here, $H_{\mathrm{D}}$ corresponds to the dot Hamiltonian and it is given by $H_{\mathrm{D}} = \varepsilon_0 \sum_\sigma d_\sigma^\dagger d_\sigma$, where $d_\sigma^\dagger$ creates an electron in the dot level with spin $\sigma =\uparrow,\downarrow$ at energy $\varepsilon_0$. The leads and couplings are described by

$$\begin{aligned} H_{\mathrm{S}}^{(j)} &= \sum\nolimits_{\boldsymbol{k}\sigma} \xi_{\boldsymbol{k}}\, c_{j\boldsymbol{k}\sigma}^\dagger c_{j\boldsymbol{k}\sigma} \\ &\quad + \Delta \sum\nolimits_{\boldsymbol{k}} \left[ e^{i\varphi_j} c_{j\boldsymbol{k}\uparrow}^\dagger c_{j(-\boldsymbol{k})\downarrow}^\dagger + \mathrm{H.c.}\right], && (2a) \\ H_{\mathrm{S-D}}^{(j)} &= w \sum\nolimits_{\boldsymbol{k}\sigma} \left[ c_{j\boldsymbol{k}\sigma}^\dagger d_\sigma + d_\sigma^\dagger c_{j\boldsymbol{k}\sigma}\right], && (2b) \\ H_{\mathrm{S-S}}^{(j,j+1)} &= t \sum\nolimits_{\boldsymbol{k}\sigma} \left[ c_{j\boldsymbol{k}\sigma}^\dagger c_{(j+1)\boldsymbol{k}\sigma} + \mathrm{H.c.}\right], && (2c) \end{aligned}$$

where $H_{\mathrm{S}}^{(j)}$ is the Hamiltonian of the $j$-th SC lead, $H_{\mathrm{S-D}}^{(j)}$ is the coupling between the $j$-th SC lead and the dot with coupling strength $w$ and $H_{\mathrm{S-S}}^{(j,j+1)}$ describes the coupling between neighboring SC leads ($j = 4 \Rightarrow j + 1 = 1$) which is assumed to be weak, i.e. $t \ll w$. Moreover, $c_{j\boldsymbol{k}\sigma}^\dagger$ creates an electronic state in lead $j$ with quasi-momentum $\boldsymbol{k}$ and spin $\sigma =\uparrow,\downarrow$ at energy $\xi_{\boldsymbol{k}} = \hbar^2\boldsymbol{k}^2/2m_{\mathrm{e}} - \mu$, where $m_{\mathrm{e}}$ is the mass of the electrons. The abbreviation H.c. is used for the Hermitian conjugate of the pervious term. We assume that all leads have the same absolute value of the SC gap $\Delta$, the same chemical potential $\mu$, but they differ in the SC phase denoted by $\varphi_j$.

As a next step, we derive the effective low-energy Hamiltonian of the dot in the presence of all SC leads. Due to proximity-induced superconductivity, the excitations on the dot are superpositions of particles and holes, the so-called Bogoliubov quasiparticles, forming ABS at energies below the SC gap. As shown in the Supplementary Materials (SM) in Section S1, in the large-gap limit $\Delta \to \infty$ and in linear order in the ratio $t/w$, the effective Hamiltonian describing the pair of ABS on the dot adopts the form $H_0 = \boldsymbol{d} \cdot \boldsymbol{\tau}$, where the three-dimensional vector $\boldsymbol{d} = (d_1, d_2, d_3)^{\mathrm{T}}$ is given by

$$\boldsymbol{d} = \begin{pmatrix} \Gamma\sum_{j=1}^{4} \cos\varphi_j \\ -\Gamma\sum_{j=1}^{4}\sin\varphi_j \\ \varepsilon_0 - 2t_0\Gamma\sum_{j=1}^{4}\cos(\varphi_j-\varphi_{j+1})\end{pmatrix}. \tag{3}$$

Here, $\Gamma = \pi N_0 w^2$, $t_0 = \pi N_0 t$, where $N_0$ is the normal density of states in the leads at the Fermi level and $\boldsymbol{\tau} = (\tau_1, \tau_2, \tau_3)^{\mathrm{T}}$ is a set of Pauli matrices in particle-hole space. Formally, this Hamiltonian has the form of a pseudo-spin $\boldsymbol{\tau}$ in an effective magnetic field $\boldsymbol{d}$, which can be controlled by the different superconducting phases $\varphi_j$.

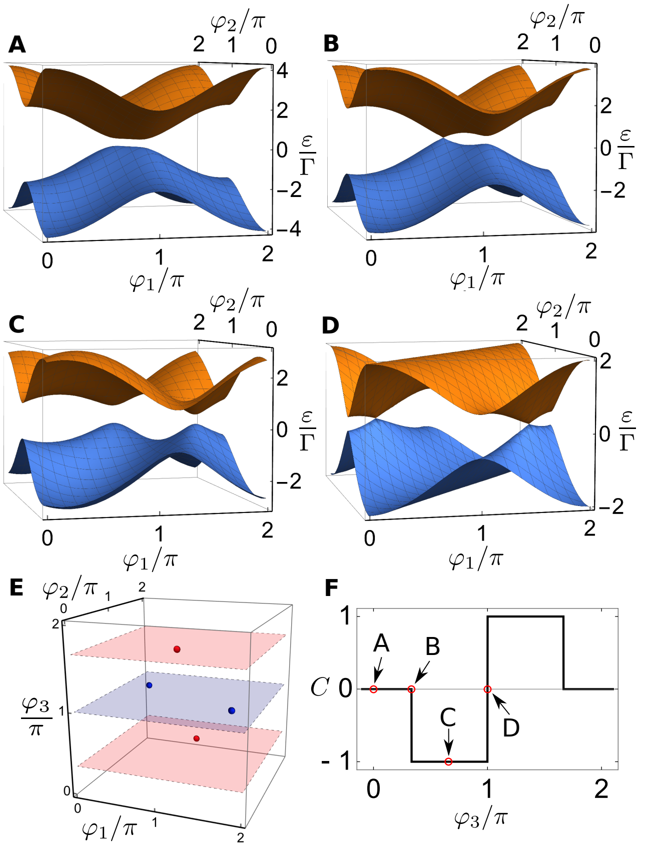

Figure 2. *Band structure, Weyl nodes and Chern number in the 4-terminal junction.* **(A-D)** Energy spectrum $\varepsilon_{\mathrm{e/g}} = \pm d$ for **(A)** $\varphi_3 = 0$, **(B)** $\varphi_3 = \pi/3$, **(C)** $\varphi_3 = 2\pi/3$, **(D)** $\varphi_3 = \pi$, respectively. **(E)** Locations of the four Weyl nodes in the FBZ. Blue (red) Weyl nodes carry a topological charge $c = +1$ $(c = -1)$, see Supplementary Materials for details. The Chern number becomes nontrivial only if the $(\varphi_1, \varphi_2)$-plane of integration lies between two opposing charges. **(F)** Chern number $C$ as a function of $\varphi_3$. The points A,B,C and D correspond to the values of $\varphi_3$ in panels **(A)**, **(B)**, **(C)** and **(D)**, respectively. Common parameters for all panels: $t_0 = 0.1$, $\varepsilon_0/\Gamma = -0.2$.

## B. Andreev bound states, Weyl nodes and Chern number

Let us show now that the Andreev spectrum of our 4-terminal system can actually exhibit Weyl nodes. The effective low-energy Hamiltonian $H_0$ defines a two-level system with a ground state (GS) $|\mathrm{g}\rangle$ and an excited state $|\mathrm{e}\rangle$, where $H_0\,|\mathrm{e/g}\rangle = \varepsilon_{\mathrm{e/g}}\,|\mathrm{e/g}\rangle$. The pair of ABS has energies given by $\varepsilon_{\mathrm{e/g}} = \pm d$, where $d = \sqrt{d_1^2 + d_2^2 + d_3^2}$ is the absolute value of the effective magnetic field. In a SC 4-terminal junction only three phases are independent and, therefore, gauge invariance allows us to set one SC phase to zero (from now on we set $\varphi_4 = 0$). The remaining three SC phases $\boldsymbol{\varphi} = (\varphi_1, \varphi_2, \varphi_3) \in [0, 2\pi)^3$ define a first Brillouin zone (FBZ) in analogy to the quasi-momentum space of a periodic crystal, which together with periodic boundary conditions form a three-torus $\mathbb{T}^3$. The spectrum $\varepsilon_{\mathrm{e/g}} = \pm d$ is shown in Figure 2A-D for several values of $\varphi_3$ from which we see that there exist zero-energy bound states which separate different gapped phases. From the constraint $d(\boldsymbol{\varphi}_{\mathrm{W}}) = 0$, we find that Weyl nodes only appear if $-8 \le m \le 0$ with $m = \varepsilon_0/t_0\Gamma$. In our case, there are four Weyl nodes $\boldsymbol{\varphi}_{\mathrm{W}}^{(s)} = (\varphi_{\mathrm{W},1}^{(s)}, \varphi_{\mathrm{W},2}^{(s)}, \varphi_{\mathrm{W},3}^{(s)})$, with $s = 1, 2, 3, 4$, which are located at (modulo $2\pi$ in each direction)

$$\boldsymbol{\varphi}_{\mathrm{W}}^{(1)} = \big(-\delta, \pi - \delta, \pi\big), \tag{4a}$$

$$\boldsymbol{\varphi}_{\mathrm{W}}^{(2)} = \big(\delta, \delta - \pi, \pi\big), \tag{4b}$$

$$\boldsymbol{\varphi}_{\mathrm{W}}^{(3)} = \big(\pi, \pi - \delta, -\delta\big), \tag{4c}$$

$$\boldsymbol{\varphi}_{\mathrm{W}}^{(4)} = \big(\pi, \delta - \pi, \delta\big), \tag{4d}$$

where $\delta = \arccos(1 + m/4)$. The locations of these zero-energy bound states in the space of SC phases are shown in Figure 2E. Each Weyl point carries a topologically positive or negative charge[34]. The sign of each charge is revealed by linearization of the Hamiltonian $H_0$ around a Weyl node, which is shown in the SM in Section S2. At this stage, we want to emphasize that the existence of zero-energy solutions $\boldsymbol{\varphi}_{\mathrm{W}}^{(s)}$ is crucially linked to the existence of a hopping $t \neq 0$ which directly connects the leads and, hence, allows for different interfering paths for particles between every two leads. In the absence of these paths (i.e. $t = 0$), the gap between the ABS cannot be closed for any $\varepsilon_0 \neq 0$ and, hence, the system stays topologically trivial.

The information about the Chern number of the GS manifold is encoded in the gauge-invariant field strength $F_{jk} = \partial_{\varphi_j} A_k - \partial_{\varphi_k} A_j$, called the Berry curvature, which is calculated from the expressions of the GS wave functions $|\mathrm{g}\rangle$ via the $U(1)$ gauge potential $A_j = i\,\langle \mathrm{g}|\partial_{\varphi_j}\mathrm{g}\rangle$, known as the Berry connection[4], which we can define due to $U(1)$ gauge symmetry of the states $|\mathrm{e/g}\rangle$. A similar calculation can be done for the excited state $|\mathrm{e}\rangle$ which contains the same information since the ABS come in particle-hole symmetric pairs.

The Berry connection gives rise to the geometric Berry phase $\varphi_{\mathrm{B}} = \oint_P \sum_j A_j \mathrm{d}\varphi_j$ if the GS is adiabatically evolved along a closed path $P$ in the space of SC phases[24].

For our particular two-level Hamiltonian $H_0$, the Berry curvature of the GS in the gapped phase ($d > 0$) can be expressed as[2]

$$F_{jk}(\boldsymbol{\varphi}) = \frac{1}{2}\Big(\boldsymbol{n} \cdot [(\partial_{\varphi_j}\boldsymbol{n}) \times (\partial_{\varphi_k}\boldsymbol{n})]\Big), \tag{5}$$

where $\boldsymbol{n} = \boldsymbol{d}/d$ is the normalized effective magnetic field. The steps to obtain this formula are provided in the SM in Section S3.

For any fixed $\varphi_3$, we can define a Chern number by integration of the Berry curvature $F_{12}(\boldsymbol{\varphi})$ over the two-torus $\mathbb{T}^2$, i.e.

$$C(\varphi_3) = \frac{1}{2\pi}\int_0^{2\pi}\mathrm{d}\varphi_1 \int_0^{2\pi}\mathrm{d}\varphi_2\, F_{12}(\boldsymbol{\varphi}), \tag{6}$$

which counts how often the unit vector $\boldsymbol{n}$ wraps around a unit sphere as a function of the remaining SC phase $\varphi_3$. Figure 2F shows that there are topologically nontrivial regions with nonzero Chern number for certain values of $\varphi_3$. The Chern number changes by $\pm 1$ for each Weyl node which is crossed while moving the $(\varphi_1, \varphi_2)$-plane of integration along the $\varphi_3$-axis. Therefore, the finite jumps of $C$ are associated with the values $\varphi_{\mathrm{W},3} = \pi$ and $\varphi_{\mathrm{W},3} = \pm\delta$. In the shown case for $m = -2$ in Figures 2E and 2F, the three values of a topological phase transition are $\varphi_{\mathrm{W},3} = \pi/3, \pi, 5\pi/3$ in the FBZ. The sign of the change of $C$ by $\pm 1$ depends on the sign of the topological charge of the Weyl point which is crossed while moving the $(\varphi_1, \varphi_2)$-plane in $\varphi_3$ direction.

### C. Microwave spectroscopy and quantum geometric tensor

Now, our goal is to show that a microwave spectroscopy allows us to obtain the full information about the topological nature of the ABS spectrum contained in the quantum geometric tensor (QGT). Let us recall that the gauge-invariant QGT of the GS is defined as[24]

$$\chi_{jk} = \left\langle \partial_{\varphi_j}\mathrm{g}\middle| \big(1 - |\mathrm{g}\rangle\langle\mathrm{g}|\big) \middle| \partial_{\varphi_k}\mathrm{g}\right\rangle, \tag{7}$$

which is Hermitian and contains information about the metric tensor $g_{jk} = \mathrm{Re}(\chi_{jk})$ and the Berry curvature $F_{jk} = -2\,\mathrm{Im}(\chi_{jk})$. Similar to Eq. 5 for the Berry curvature, also the metric tensor $g_{jk}$ can be conviniently calculated from the normalized effective magnetic field $\boldsymbol{n} = \boldsymbol{d}/d$ via

$$g_{jk} = \frac{1}{4}(\partial_{\varphi_j}\boldsymbol{n}) \cdot (\partial_{\varphi_k}\boldsymbol{n}), \tag{8}$$

which is derived in the SM in Section S3. As we proceed to show, these quantities can be measured experimentally by application of a small time-periodic modulation of the phases.

Let us first show how the diagonal components of the geometric tensor, $\chi_{jj} = g_{jj}$, can be obtained. For this purpose, we modulate one of the SC phases according to $\varphi_j \to \varphi_j + (2A/\hbar\omega)\cos(\omega t)$, with a frequency $\omega$ and for $(A/\hbar\omega) \ll 1$ (see Figure 1B), where $A$ is a coupling parameter, $\hbar$ is Planck's constant and $t$ is the time. The resulting Hamiltonian in linear order becomes

$$H = H_0 + \frac{2A}{\hbar\omega}\frac{\partial H_0}{\partial\varphi_j}\cos(\omega t) \tag{9}$$

from which we obtain the transition rate between the two states

$$R_{jj} = \frac{2\pi A^2}{\hbar^4\omega^2}\left|\langle\mathrm{e}|\,\frac{\partial H_0}{\partial\varphi_j}\,|\mathrm{g}\rangle\right|^2 \delta(2d/\hbar - \omega) \tag{10}$$

by applying Fermi's golden rule (see Figure 1C). From integrating out the frequency follows

$$\bar{R}_{jj} = \int_0^\infty \mathrm{d}\omega\, R_{jj} = \frac{2\pi A^2}{\hbar^2} g_{jj}, \tag{11}$$

which is nothing but the weight of the resonance at $\hbar\omega = 2d$ obtained from integrating the $\delta$-function in Eq. 10. The details of the derivation of this result are presented in the SM in Section S4. Note that Eq. 11 is generally valid even in the presence of a finite broadening of the line, as it is expected in real situations.

Let us now show that the off-diagonal elements are obtained by time-periodic modulation of two phases (see Figure 1B). Depending on the relative phase difference $\gamma$ between both modulations, one obtains information about the off-diagonal elements of the QGT $\chi_{jk} = g_{jk} - iF_{jk}/2$. For $j \neq k$, we use the modulations (see Figure 1D)

$$\varphi_j \to \varphi_j + (2A/\hbar\omega)\cos(\omega t), \tag{12a}$$

$$\varphi_k \to \varphi_k + (2A/\hbar\omega)\cos(\omega t - \gamma), \tag{12b}$$

where we again assume $(A/\hbar\omega) \ll 1$. Analogue to Eq. 9, we obtain the Hamiltonian in linear order

$$H = H_0 + \frac{2A}{\hbar\omega}\left(\frac{\partial H_0}{\partial\varphi_j}\cos(\omega t) + \frac{\partial H_0}{\partial\varphi_k}\cos(\omega t - \gamma)\right), \tag{13}$$

from which we obtain the transition rates via Fermi's golden rule

$$R_{jk}^{(\gamma)} = \frac{2\pi A^2}{\hbar^4\omega^2}\left|\langle\mathrm{e}|\left(\frac{\partial H_0}{\partial\varphi_j} + e^{i\gamma}\frac{\partial H_0}{\partial\varphi_k}\right)|\mathrm{g}\rangle\right|^2 \delta(2d/\hbar - \omega). \tag{14}$$

Now, it can be shown that by performing two subsequent measurements with $\gamma_1 = 0$ and $\gamma_2 = \pi$ (orthogonal linear polarizations), we can extract the off-diagonal part of the metric tensor $g_{jk}$, while two measurements with $\gamma_1 = \pi/2$ and $\gamma_2 = -\pi/2$ (right-/left-handed circular polarization) can be used to measure the Berry curvature $F_{jk}$. For this purpose, and following Eq. 11, we define the amplitudes of the rates at resonance $\bar{R}_{jk}^{(\gamma)} = \int_0^\infty \mathrm{d}\omega\ R_{jk}^{(\gamma)}$, which,

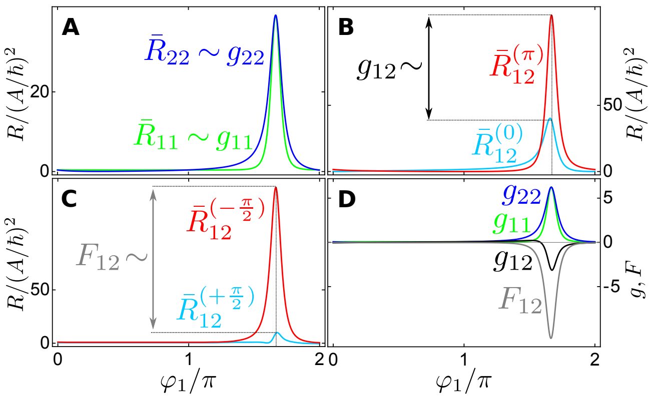

Figure 3. *Transition rates and elements of the quantum geometric tensor.* From the measured transition rates $R$ via microwave spectroscopy, we can extract the elements of the quantum geometric tensor $\chi_{jk} = g_{jk} - iF_{jk}/2$. **(A)** The integrated rates $\bar{R}_{jj}$ are proportional to the diagonal parts of the metric $g_{jj}$ (Eq. 11). **(B)** The difference between the integrated rates $\bar{R}_{jk}^{(\gamma)}$ obtained by driving two phases with linear polarizations ($\gamma = 0, \pi$) is proportional to the off-diagonal parts of the metric $g_{jk}$ (Eq. 15a). **(C)** The difference between the integrated rates $R_{jk}^{(\gamma)}$ obtained by driving two phases with circular polarizations ($\gamma = \pm\pi/2$) is proportional to the Berry curvature $F_{jk}$ (Eq. 15b). **(D)** Results for the extracted components of the quantum metric $g$ and the Berry curvature $F$. Common parameters for all panels: $\varphi_2 = \pi$, $\varphi_3 = 2\pi/3$, $t_0 = 0.1$, $\varepsilon_0/\Gamma = -2$.

as shown in the SM in Section S4, satisfy the following relations:

$$\bar{R}_{jk}^{(0)} - \bar{R}_{jk}^{(\pi)} = \frac{8\pi A^2}{\hbar^2}\, g_{jk}, \tag{15a}$$

$$\bar{R}_{jk}^{(+\frac{\pi}{2})} - \bar{R}_{jk}^{(-\frac{\pi}{2})} = \frac{4\pi A^2}{\hbar^2}\, F_{jk}. \tag{15b}$$

Therefore, the full QGT $\chi_{jk}$ of the GS is extracted from the amplitudes at resonance via periodic modulation of different SC phases. All these relations are summarized in Figure 3 for a cut with fixed $\varphi_2$ in the topologically nontrivial region with Chern number $C = -1$.

Let us summarize the driving protocols. First, the modulation of a single phase $\varphi_j$ enables the extraction of the diagonal elements $g_{jj}$ of the metric tensor directly from the rate amplitudes at resonance (Figure 3A). Second, the off-diagonal elements of the metric tensor $g_{jk}$ can be obtained by driving two different phases and using orthogonal linear polarizations (Figure 3B). Similarly, by using orthogonal circular polarized drives on the same phases, we can extract the Berry curvature $F_{jk}$ from the differences between the rate amplitudes of the resulting responses (Figure 3C). The resulting elements of the QGT $\chi_{jk}$ are shown in Figure 3D. Finally, let us recall that once the Berry curvature $F_{jk}$ is extracted, the Chern number $C$ automatically follows from an integration of $F_{jk}$ over the corresponding two SC phases $\varphi_j$ and $\varphi_k$, see Eq. 6.

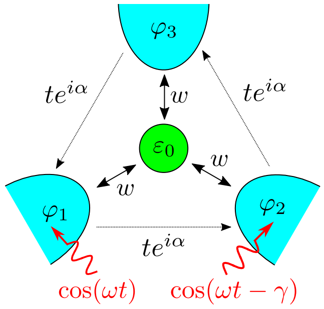

Figure 4. *Microscopic model of the 3-terminal Josephson junction.* Three superconducting leads, each with a pairing phase $\varphi_j$ ($j = 1, 2, 3$), are connected to a normal quantum dot with level $\varepsilon_0$ via the couplings $w$ and leads are directly connected to each other by the couplings $t \ll w$. There is a magnetic flux of $\Phi = 3\alpha\Phi_0$ (flux quantum $\Phi_0 = \hbar/2e$) in the normal region of the junction modifying the hopping $t$ by a phase factor $e^{i\alpha}$ in counter-clockwise direction. Phases $\varphi_1$ and $\varphi_2$ are modulated at frequency $\omega$ to obtain the Chern number $C$ as a function of $\alpha$ (for $\varphi_3 = 0$), where $\gamma$ is the relative phase between both modulations.

## III. DISCUSSION

We have presented a procedure to have full access to the quantum geometric tensor of topological Josephson matter through a generalized microwave spectroscopy in which different artificial polarizations of the drives are used. So far, we have discussed the specific case of a 4-terminal junction, but actually, this method can be universally applied to any multiterminal Josephson device. Thus, for instance, we show in Figure 4 another possible realization of topological Josephson matter that is discussed in detail in the SM in Section S5. In this case, the system comprises three superconducting terminals and the normal region is subjected to a perpendicular magnetic field enclosing a magnetic flux $\Phi$. As shown in Ref. [21], this type of system also supports Weyl nodes as long as there is a finite direct coupling between the neighboring leads. In the SM we show that the low-energy physics in the dot is again described by an effective Hamiltonian of the form $H_0 = \boldsymbol{d} \cdot \boldsymbol{\tau}$ and the microwave spectroscopy can be used in exactly the same way as in the previous example to extract the full information about the quantum geometric tensor. Again, the presence of the direct link between the superconductors is essential to obtain nontrivial topology.

Since these effects occuring in multiterminal Josephson devices are discussed in the low-energy limit, they should be, in principle, experimentally accessible by microwave spectroscopy. In analogy to topological insulators, the superconducting phases play the role of quasi-momenta that can be controlled by SQUID loops[23] and the modulation of superconducting phases can be performed by varying the magnetic fluxes in the SQUID loops with a small ac drive[9–12]. We emphasize that our proposed method is an alternative scheme to detect the topological properties beyond the previously suggested transconductance measurements[13] with the possible advantage that no electronic contacts are needed.

To conclude, we emphasize the universal nature of our proposal, which can be applied to various kinds of topological Josephson matter. As long as two superconducting phases can be addressed independently, the quantum geometric tensor can be determined by engineering the phase difference as we have described. This offers a new avenue for microwave-based characterization of quantum states in superconducting nanostructures. It will be interesting to apply our method to proposed topologically protected candidates for quantum information hardware in superconductors, like e.g. Majorana states[35] or parafermions[36]. A further direction might be to address Coulomb interactions on the quantum dot between superconductors[37], but this goes beyond the scope of the present article.

## ACKNOWLEDGMENTS

We thank Robert Hussein for useful discussions. This work was supported by the DFG through SFB 767 and Grant No. RA 2810/1. J.C.C. acknowledges the support via the Mercator Program of the DFG in the frame of the SFB 767.

---

[1] C. L. Kane and E. J. Mele, Phys. Rev. Lett. **95**, 146802 (2005).

[2] M. Z. Hasan and C. L. Kane, Rev. Mod. Phys. **82**, 3045 (2010).

[3] N. P. Armitage, E. J. Mele, and A. Vishwanath, Rev. Mod. Phys. **90**, 015001 (2018).

[4] M. V. Berry, Proc. R. Soc. London, Ser. A **392**, 45 (1984).

[5] M. Sato and Y. Ando, Rep. Prog. Phys. **80**, 076501 (2017).

[6] A. Bansil, H. Lin, and T. Das, Rev. Mod. Phys. **88**, 021004 (2016).

[7] N. M. Chtchelkatchev and Y. V. Nazarov, Phys. Rev. Lett. **90**, 226806 (2003).

[8] A. Zazunov, V. S. Shumeiko, E. N. Bratus, J. Lantz, and G. Wendin, Phys. Rev. Lett. **90**, 087003 (2003).

[9] L. Bretheau, Ç. Ö. Girit, H. Pothier, D. Esteve, and C. Urbina, Nature **499**, 312 (2013).

[10] C. Janvier, L. Tosi, L. Bretheau, Ç. Ö. Girit, M. Stern, P. Bertet, P. Joyez, D. Vion, D. Esteve, M. F. Goffman, H. Pothier, and C. Urbina, Science **349**, 1199 (2015).

[11] D. J. van Woerkom, A. Proutski, B. van Heck, D. Bouman, J. I. Väyrynen, L. I. Glazman, P. Krogstrup, J. Nygård, L. P. Kouwenhoven, and A. Geresdi, Nat. Phys. **13**, 876 (2017).

[12] L. Bretheau, Ç. Ö. Girit, C. Urbina, D. Esteve, and H. Pothier, Phys. Rev. X **3**, 041034 (2013).

[13] R.-P. Riwar, M. Houzet, J. S. Meyer, and Y. V. Nazarov, Nat. Commun. **7**, 11167 (2016).

[14] T. Yokoyama and Y. V. Nazarov, Phys. Rev. B **92**, 155437 (2015).

[15] T. Yokoyama, J. Reutlinger, W. Belzig, and Y. V. Nazarov, Phys. Rev. B **95**, 045411 (2017).

[16] E. Eriksson, R.-P. Riwar, M. Houzet, J. S. Meyer, and Y. V. Nazarov, Phys. Rev. B **95**, 075417 (2017).

[17] H.-Y. Xie, M. G. Vavilov, and A. Levchenko, Phys. Rev. B **97**, 035443 (2018).

[18] B. van Heck, S. Mi, and A. R. Akhmerov, Phys. Rev. B **90**, 155450 (2014).

[19] C. Padurariu, T. Jonckheere, J. Rech, R. Mélin, D. Feinberg, T. Martin, and Y. V. Nazarov, Phys. Rev. B **92**, 205409 (2015).

[20] H.-Y. Xie, M. G. Vavilov, and A. Levchenko, Phys. Rev. B **96**, 161406 (2017).

[21] J. S. Meyer and M. Houzet, Phys. Rev. Lett. **119**, 136807 (2017).

[22] S. R. Plissard, I. van Weperen, D. Car, M. A. Verheijen, G. W. G. Immink, J. Kammhuber, L. J. Cornelissen, D. B. Szombati, A. Geresdi, S. M. Frolov, L. P. Kouwenhoven, and E. P. A. M. Bakkers, Nat. Nanotechnol. **8**, 859 (2013).

[23] E. Strambini, S. D'Ambrosio, F. Vischi, F. S. Bergeret, Y. V. Nazarov, and F. Giazotto, Nat. Nanotechnol. **11**, 1055 (2016).

[24] M. Kolodrubetz, D. Sels, P. Mehta, and A. Polkovnikov, Phys. Rep. **697**, 1 (2017).

[25] T. Neupert, C. Chamon, and C. Mudry, Phys. Rev. B **87**, 245103 (2013).

[26] M. Kolodrubetz, V. Gritsev, and A. Polkovnikov, Phys. Rev. B **88**, 064304 (2013).

[27] T. Ozawa and N. Goldman, Phys. Rev. B **97**, 201117 (2018).

[28] D. T. Tran, A. Dauphin, A. G. Grushin, P. Zoller, and N. Goldman, Sci. Adv. **3**, e1701207 (2017).

[29] D. T. Tran, N. R. Cooper, and N. Goldman, Phys. Rev. A **97**, 061602 (2018).

[30] N. Fläschner, B. S. Rem, M. Tarnowski, D. Vogel, D. S. Lühmann, K. Sengstock, and C. Weitenberg, Science **352**, 1091 (2016).

[31] L. Asteria, D. T. Tran, T. Ozawa, M. Tarnowski, B. S. Rem, N. Fläschner, K. Sengstock, N. Goldman, and C. Weitenberg, arXiv:1805.11077 [cond-mat.quant-gas] (2018).

[32] X. Tan, D.-W. Zhang, Q. Liu, G. Xue, H.-F. Yu, Y.-Q. Zhu, H. Yan, S.-L. Zhu, and Y. Yu, Phys. Rev. Lett. **120**, 130503 (2018).

[33] M. Wimmer, H. M. Price, I. Carusotto, and U. Peschel, Nat. Phys. **13**, 545 (2017).

[34] X. Wan, A. M. Turner, A. Vishwanath, and S. Y. Savrasov, Phys. Rev. B **83**, 205101 (2011).

[35] A. Y. Kitaev, Phys. Usp. **44**, 131 (2001).

[36] J. Klinovaja, A. Yacoby, and D. Loss, Phys. Rev. B **90**, 155447 (2014).

[37] P. Marra, A. Braggio, and R. Citro, Beilstein J. Nanotechnol. **9**, 1705 (2018).

## SUPPLEMENTARY MATERIALS

### Section S1. Effective low-energy Hamiltonian: 4-terminal junction

In this section, we derive the effective low-energy Hamiltonian of the dot in the presence of the superconducting leads. By introducing spinors in Nambu space $\Psi^\dagger_{j\boldsymbol{k}} = (c^\dagger_{j\boldsymbol{k}\uparrow}, c_{j(-\boldsymbol{k})\downarrow})$ for the leads ($j = 1,2,3,4$) and $\Psi^\dagger_\mathrm{D} = (d^\dagger_\uparrow, d_\downarrow)$, we rewrite the unperturbed Hamiltonians as $H^{(j)}_\mathrm{S} = \sum_{\boldsymbol{k}} \Psi^\dagger_{j\boldsymbol{k}} \hat{H}_{\mathrm{S},j\boldsymbol{k}} \Psi_{j\boldsymbol{k}}$ and $H_\mathrm{D} = \Psi^\dagger_\mathrm{D} \hat{H}_\mathrm{D} \Psi_\mathrm{D}$, respectively, with $\hat{H}_{\mathrm{S},j\boldsymbol{k}} = \xi_{\boldsymbol{k}}\tau_3 + \Delta e^{i\varphi_j\tau_3}\tau_1$ and $\hat{H}_\mathrm{D} = \varepsilon_0\tau_3$ and the Pauli matrices $\tau_1, \tau_2$ and $\tau_3$ in Nambu space. Note that due to isotropic symmetry $\xi_{\boldsymbol{k}} = \xi_{-\boldsymbol{k}}$ holds, which we have already used.

From $\hat{g}_{j\boldsymbol{k}} = (\varepsilon - \hat{H}_{\mathrm{S},j\boldsymbol{k}})^{-1}$, we obtain the bare Green's function (GF) of the $j$-th lead

$$\hat{g}_{j\boldsymbol{k}} = \frac{\varepsilon - \xi_{\boldsymbol{k}}\tau_3 + \Delta e^{i\varphi_j\tau_3}\tau_1}{\varepsilon^2 - \xi^2_{\boldsymbol{k}} - \Delta^2}. \tag{SM1}$$

Since the tunneling matrix elements $t$ and $w$ do not depend on quasi-momentum $\boldsymbol{k}$, we can already sum over all quasi-momenta to obtain the new GF of the lead $\hat{g}_j = \sum_{\boldsymbol{k}} \hat{g}_{j\boldsymbol{k}}$. Turning the summation over $\boldsymbol{k}$ into an integration over energies in the wide-band limit via $\sum_{\boldsymbol{k}} \to N_0 \int \mathrm{d}\xi_{\boldsymbol{k}}$, where $N_0$ is the normal state density of states at the Fermi energy, we obtain

$$\hat{g}_j = -\pi N_0 \frac{\varepsilon + \Delta e^{i\varphi_j\tau_3}\tau_1}{\sqrt{\Delta^2 - \varepsilon^2}} \quad \xrightarrow{\Delta\to\infty} \quad -\pi N_0 e^{i\varphi_j\tau_3}\tau_1 \tag{SM2}$$

defined in the local basis $\Psi^\dagger_j = (c^\dagger_{j\uparrow}, c_{j\downarrow})$, where we assume $\Delta$ to be larger than all relevant energies in the system. The GF of the bare dot is given by $\hat{g}_\mathrm{D} = 1/(\varepsilon - \varepsilon_0\tau_3)$. From the Hamiltonian describing the hopping between the $j$-th lead and the dot we obtain $\hat{V}_{j\mathrm{D}} = w\tau_3$, while we obtain for the coupling between the $j$-th and $(j+1)$-th lead $\hat{V}_{j(j+1)} = t\tau_3$. By means of Dyson's equation $G = g + gVG$, where $G$ is the dressed GF of the total system, we find the system of coupled equations ($j = 1,2,3,4$)

$$\hat{G}_{j\mathrm{D}} = \hat{g}_1\tau_3 \left( t\,\hat{G}_{(j+1)\mathrm{D}} + t\,\hat{G}_{(j+3)\mathrm{D}} + w\hat{G}_\mathrm{D} \right) \tag{SM3a}$$

$$\hat{G}_\mathrm{D} = \hat{g}_\mathrm{D} + w\,\hat{g}_\mathrm{D}\tau_3 \sum\nolimits_j \hat{G}_{j\mathrm{D}}, \tag{SM3b}$$

which we solve for the dressed GF of the dot to linear order in $t$ and obtain

$$\hat{G}^{-1}_\mathrm{D} = \hat{g}^{-1}_\mathrm{D} - \hat{\Sigma}_\mathrm{D}, \tag{SM4}$$

with the self-energy

$$\hat{\Sigma}_\mathrm{D} = -w^2 \Big[ \sum_{j=1}^{4} \hat{g}_j - t(\hat{g}_1 + \hat{g}_3)\tau_3(\hat{g}_2 + \hat{g}_4) - t(\hat{g}_2 + \hat{g}_4)\tau_3(\hat{g}_1 + \hat{g}_3) \Big] + \mathcal{O}(t^2). \tag{SM5}$$

From the self-energy, we obtain the effective low-energy Hamiltonian $H_0$ of the dot as

$$H_0 = \varepsilon - \hat{G}^{-1}_\mathrm{D} = \varepsilon - \hat{g}^{-1}_\mathrm{D} + \hat{\Sigma}_\mathrm{D} = \varepsilon_0\tau_3 + \hat{\Sigma}_\mathrm{D}, \tag{SM6}$$

which can be written as $H_0 = \boldsymbol{d}\cdot\boldsymbol{\tau}$, with the pseudo-spin $\boldsymbol{\tau}$ (set of Pauli matrices in Nambu space) and the effective magnetic field $\boldsymbol{d}$ as presented in Eq. 3 in the main text. This two-level Hamiltonian has a ground state $|\mathrm{g}\rangle$ and an excited state $|\mathrm{e}\rangle$ which satisfy $H_0\,|\mathrm{e/g}\rangle = \varepsilon_{\mathrm{e/g}}\,|\mathrm{e/g}\rangle$, with the eigenenergies $\varepsilon_{\mathrm{e/g}} = \pm d$ and the absolute value of the effective field $d = \sqrt{d_1^2 + d_2^2 + d_3^2}$. The eigenstates are given by

$$\begin{aligned} |\mathrm{e/g}\rangle &= \frac{1}{\sqrt{2d(d \mp d_3)}} \begin{pmatrix} d_1 - id_2 \\ \pm d - d_3 \end{pmatrix} \\ &= \frac{1}{\sqrt{2 \mp 2\cos\theta}} \begin{pmatrix} e^{-i\varphi}\sin\theta \\ \pm 1 - \cos\theta \end{pmatrix}, \end{aligned} \tag{SM7}$$

where the spherical angles $\theta \in [0,\pi)$ and $\varphi \in [0, 2\pi)$ are defined by the set of equations

$$\begin{aligned} \cos\varphi &= \frac{d_1}{\sqrt{d_1^2 + d_2^2}}, \quad \cos\theta = \frac{d_3}{d}, \\ \sin\varphi &= \frac{d_2}{\sqrt{d_1^2 + d_2^2}}, \quad \sin\theta = \frac{\sqrt{d_1^2 + d_2^2}}{d}, \end{aligned} \tag{SM8}$$

which parametrize the Bloch sphere. This explicitly shows that the eigenstates are independent of the absolute value $d$ of the effective field.

### Section S2. Topological charge of the Weyl points

Here, we describe how to obtain the sign of the topological charge of the four Weyl points. We focus on the 4-terminal junctions discussed in the main text. In the vincinity of one of the points of degeneracy $\boldsymbol{\varphi}^{(s)}_\mathrm{W} = (\varphi^{(s)}_{\mathrm{W},1}, \varphi^{(s)}_{\mathrm{W},2}, \varphi^{(s)}_{\mathrm{W},3})$ for $s = 1,2,3,4$, we linearize the spectrum via the replacement $\varphi_k = \varphi^{(s)}_{\mathrm{W},k} + \delta\varphi_k$ for $k = 1,2,3$, where $\delta\varphi_k$ is a small deviation from the Weyl point in the direction of $\varphi_k$. Since for all Weyl points $d(\boldsymbol{\varphi}^{(s)}_\mathrm{W}) = 0$ holds, we obtain $\boldsymbol{d} = \boldsymbol{M}^{(s)}\boldsymbol{\delta\varphi}$ with $\boldsymbol{\delta\varphi} = (\delta\varphi_1, \delta\varphi_2, \delta\varphi_3)^\mathrm{T}$ and the elements

$$M^{(s)}_{1k} = -\Gamma\sin\varphi^{(s)}_{\mathrm{W},k}, \tag{SM9a}$$

$$M^{(s)}_{2k} = -\Gamma\cos\varphi^{(s)}_{\mathrm{W},k}, \tag{SM9b}$$

$$M^{(s)}_{31} = 2\Gamma t_0[\sin(\varphi^{(s)}_{\mathrm{W},1} - \varphi^{(s)}_{\mathrm{W},2}) + \sin(\varphi^{(s)}_{\mathrm{W},1})], \tag{SM9c}$$

$$M^{(s)}_{32} = 2\Gamma t_0[\sin(\varphi^{(s)}_{\mathrm{W},2} - \varphi^{(s)}_{\mathrm{W},3}) - \sin(\varphi^{(s)}_{\mathrm{W},1} - \varphi^{(s)}_{\mathrm{W},2})], \tag{SM9d}$$

$$M^{(s)}_{33} = 2\Gamma t_0[\sin(\varphi^{(s)}_{\mathrm{W},3}) - \sin(\varphi^{(s)}_{\mathrm{W},2} - \varphi^{(s)}_{\mathrm{W},3})], \tag{SM9e}$$

of the transformation matrix $\boldsymbol{M}^{(s)}$ which define the "velocities" $\boldsymbol{v}^{(s)}_k = (M^{(s)}_{k1}, M^{(s)}_{k2}, M^{(s)}_{k3})^\mathrm{T}$. The Weyl-Hamiltonian can then be written as

$$H^{(s)}_\mathrm{W} = \sum\nolimits_{kl} \tau_l M^{(s)}_{lk}\,\delta\varphi_k = \sum\nolimits_k (\boldsymbol{v}^{(s)}_k \cdot \boldsymbol{\delta\varphi})\tau_k. \tag{SM10}$$

The topological charge $c_s$ (or chirality) of a Weyl point is defined via $c_s = \mathrm{sgn}[\boldsymbol{v}_1^{(s)} \cdot (\boldsymbol{v}_2^{(s)} \times \boldsymbol{v}_3^{(s)})] = \mathrm{sgn}[\det(\boldsymbol{M}^{(s)})]$, where the triple product of the velocities is

$$\begin{aligned}\det(\boldsymbol{M}^{(s)}) = 2t_0\Gamma^3 \sin(\varphi_{\mathrm{W},1}^{(s)} - \varphi_{\mathrm{W},3}^{(s)})\big[\sin(\varphi_{\mathrm{W},1}^{(s)} - \varphi_{\mathrm{W},2}^{(s)}) \\ + \sin(\varphi_{\mathrm{W},2}^{(s)}) - \sin(\varphi_{\mathrm{W},2}^{(s)} - \varphi_{\mathrm{W},3}^{(s)})\big].\end{aligned} \tag{SM11}$$

From Eq. 4 in the main text, we see that we have four Weyl points in the 3D parameter space, where $\boldsymbol{\varphi}_{\mathrm{W}}^{(1,2)}$ are located in the $\varphi_3 = \pi$ plane and $\boldsymbol{\varphi}_{\mathrm{W}}^{(3,4)}$ are located in the $\varphi_1 = \pi$ plane and recall that $-8 < m < 0$ and, therefore, $\mathrm{sgn}(m) = -1$. For the four points we find $c_{1,2} = \mathrm{sgn}(t_0)$ and $c_{3,4} = -\mathrm{sgn}(t_0)$ since $\Gamma > 0$. This also follows from time-reversal symmetry which links $\boldsymbol{\varphi}_{\mathrm{W}}^{(1)} = -\boldsymbol{\varphi}_{\mathrm{W}}^{(2)}(+2\pi\boldsymbol{z})$, $\boldsymbol{z} \in \mathbb{Z}^3$, and $\boldsymbol{\varphi}_{\mathrm{W}}^{(3)} = -\boldsymbol{\varphi}_{\mathrm{W}}^{(4)}(+2\pi\boldsymbol{z})$, $\boldsymbol{z} \in \mathbb{Z}^3$. Weyl points which are linked by time-reversal symmetry must have the same charge.

## Section S3. Quantum geometric tensor from an effective magnetic field

Here, we provide explicit formulas of how to compute the Berry curvature $F_{jk}$ and the quantum metric tensor $g_{jk}$ of the ground state $|\mathrm{g}\rangle$ directly from the effective Hamiltonian $H_0 = \boldsymbol{d} \cdot \boldsymbol{\tau}$. In general, the effective field is controlled by a set of $n$ parameters $\boldsymbol{\lambda} = (\lambda_1, \ldots, \lambda_n)$, i.e. $\boldsymbol{d} = \boldsymbol{d}(\boldsymbol{\lambda})$. Using the explicit expression of $|\mathrm{g}\rangle$, see Eq. SM7, in the definition of the quantum geometric tensor of the ground state $\chi_{jk} = \langle \partial_j \mathrm{g}|(1 - |\mathrm{g}\rangle\langle\mathrm{g}|)|\partial_k \mathrm{g}\rangle$, we find

$$\begin{aligned}\chi_{jk} = \frac{1}{4}\left(\frac{\partial\theta(\boldsymbol{\lambda})}{\partial\lambda_j} + i\sin\theta(\boldsymbol{\lambda})\,\frac{\partial\varphi(\boldsymbol{\lambda})}{\partial\lambda_j}\right) \\ \times \left(\frac{\partial\theta(\boldsymbol{\lambda})}{\partial\lambda_k} - i\sin\theta(\boldsymbol{\lambda})\,\frac{\partial\varphi(\boldsymbol{\lambda})}{\partial\lambda_k}\right),\end{aligned} \tag{SM12}$$

where $\partial_j = \partial/\partial\lambda_j$. The quantum metric (i.e. the Fubini-Study metric) is given by the real part, $g_{jk} = \mathrm{Re}(\chi_{jk})$, and the Berry curvature is given by the imaginary part, $F_{jk} = -2\mathrm{Im}(\chi_{jk})$. We obtain

$$F_{jk} = \frac{1}{2}\sin\theta(\boldsymbol{\lambda})\left(\frac{\partial\theta(\boldsymbol{\lambda})}{\partial\lambda_j}\frac{\partial\varphi(\boldsymbol{\lambda})}{\partial\lambda_k} - \frac{\partial\theta(\boldsymbol{\lambda})}{\partial\lambda_k}\frac{\partial\varphi(\boldsymbol{\lambda})}{\partial\lambda_j}\right), \tag{SM13a}$$

$$g_{jk} = \frac{1}{4}\left(\frac{\partial\theta(\boldsymbol{\lambda})}{\partial\lambda_j}\frac{\partial\theta(\boldsymbol{\lambda})}{\partial\lambda_k} + \sin^2\theta(\boldsymbol{\lambda})\,\frac{\partial\varphi(\boldsymbol{\lambda})}{\partial\lambda_j}\frac{\partial\varphi(\boldsymbol{\lambda})}{\partial\lambda_k}\right). \tag{SM13b}$$

We find by differentiating Eq. SM8 with respect to $\lambda_j$:

$$\frac{\partial\varphi(\boldsymbol{\lambda})}{\partial\lambda_j} = \frac{1}{d_1^2 + d_2^2}\sum_{\alpha,\beta=1}^{2} \varepsilon_{\alpha\beta} d_\alpha \partial_j d_\beta, , \tag{SM14a}$$

$$\frac{\partial\theta(\boldsymbol{\lambda})}{\partial\lambda_j} = \frac{1}{d^2\sqrt{d_1^2 + d_2^2}}\sum_{\alpha=1}^{2} d_\alpha\left(d_3\partial_j d_\alpha - d_\alpha\partial_j d_3\right), \tag{SM14b}$$

where $\varepsilon_{\alpha\beta} = -\varepsilon_{\beta\alpha}$ is the total antisymmetric Levi-Civita tensor in two dimensions. Using Eq. SM14 in Eq. SM13a, we find that, after some algebra, the Berry curvature can be written as

$$F_{jk} = \frac{\boldsymbol{d} \cdot [(\partial_j\boldsymbol{d}) \times (\partial_k\boldsymbol{d})]}{2d^3} = \frac{1}{2}\Big(\boldsymbol{n} \cdot [(\partial_j\boldsymbol{n}) \times (\partial_k\boldsymbol{n})]\Big), \tag{SM15}$$

which allows for the computation of the Berry curvature directly from the effective magnetic field $\boldsymbol{d}$. For the second equation we introduced the normaized effective field $\boldsymbol{n} = \boldsymbol{d}/d$ which shows explicitly that the Berry curvature is independent of the absolute value $d$. A similar formula can be obtained for the quantum metric tensor. Using Eq. SM14 in Eq. SM13b, we find after some algebra

$$\begin{aligned}g_{jk} &= \frac{1}{4d^4}\bigg(d^2\Big[(\partial_j\boldsymbol{d}) \cdot (\partial_k\boldsymbol{d})\Big] - \Big[\boldsymbol{d} \cdot (\partial_j\boldsymbol{d})\Big]\ \Big[\boldsymbol{d} \cdot (\partial_k\boldsymbol{d})\Big]\bigg) \\ &= \frac{1}{4}(\partial_j\boldsymbol{n}) \cdot (\partial_k\boldsymbol{n}),\end{aligned} \tag{SM16}$$

where we used

$$\begin{aligned}\sum_{\substack{\alpha,\beta=1 \\ \alpha<\beta}}^{3} d_\alpha d_\beta\Big[(\partial_j d_\alpha)(\partial_k d_\beta) + (\partial_j d_\beta)(\partial_k d_\alpha)\Big] \\ = \Big[\boldsymbol{d} \cdot (\partial_j\boldsymbol{d})\Big]\Big[\boldsymbol{d} \cdot (\partial_k\boldsymbol{d})\Big] - \sum_{\alpha=1}^{3} d_\alpha^2(\partial_j d_\alpha)(\partial_k d_\alpha)\end{aligned} \tag{SM17}$$

to simplify the equation.

## Section S4. Quantum geometric tensor and transition rates

The effective low-energy Hamiltonian of the dot in all the realizations of topological Josephson matter discussed in this work adopts the form $H_0 = \boldsymbol{d} \cdot \boldsymbol{\tau}$. This Hamiltonian describes an effective two-level system with $H_0|\mathrm{e/g}\rangle = \varepsilon_{\mathrm{e/g}}|\mathrm{e/g}\rangle$, where $\varepsilon_{\mathrm{g}} = -d$ and $\varepsilon_{\mathrm{e}} = +d$ are the Andreev bound state (ABS) energies of the ground state (GS) $|\mathrm{g}\rangle$ and the excited state $|\mathrm{e}\rangle$, respectively. Here, $d = \sqrt{d_1^2 + d_2^2 + d_3^2}$ denotes the absolute value of $\boldsymbol{d}$.

Since the physical states have a $U(1)$ gauge degree of freedom, we define the $U(1)$ Berry connection $A_j = i\langle\mathrm{g}|\partial_{\varphi_j}\mathrm{g}\rangle$ of the GS. This gauge connection is necessary to understand the evolution of the phase of the states as one varies the parameters along a line in parameter space. Closing the line to a loop $P$, we can compute the gauge invariant Berry phase via $\varphi_{\mathrm{B}} = \oint_P \sum_j A_j \mathrm{d}\varphi_j$, where $\varphi_j$ is the superconducting phase of the lead $j$. Moreover, we obtain the gauge invariant Berry curvature as

$$F_{jk} = \partial_{\varphi_j}A_k - \partial_{\varphi_k}A_j = i\left[\langle\partial_{\varphi_j}\mathrm{g}|\partial_{\varphi_k}\mathrm{g}\rangle - \langle\partial_{\varphi_k}\mathrm{g}|\partial_{\varphi_j}\mathrm{g}\rangle\right]. \tag{SM18}$$

Furthermore, we need the relation

$$0 = \langle \mathrm{e} | (\partial_{\varphi_j} H_0) | \mathrm{g} \rangle + 2d \langle \mathrm{e} | \partial_{\varphi_j} \mathrm{g} \rangle , \tag{SM19}$$

which follows from $\partial_{\varphi_j} \langle \mathrm{e} | H_0 | \mathrm{g} \rangle = 0$. First, we proof Eq. 11 in the main text by rewriting the left-hand side

$$\begin{aligned}\bar{R}_{jj} &= \frac{2\pi A^2}{\hbar^2} \frac{\left| \langle \mathrm{e} | \left(\partial_{\varphi_j} H_0\right) | \mathrm{g} \rangle \right|^2}{(2d)^2} = \frac{2\pi A^2}{\hbar^2} \langle \partial_{\varphi_j} \mathrm{g} | \mathrm{e} \rangle \langle \mathrm{e} | \partial_{\varphi_j} \mathrm{g} \rangle \\ &= \frac{2\pi A^2}{\hbar^2} \langle \partial_{\varphi_j} \mathrm{g} | \left(1 - |\mathrm{g}\rangle \langle \mathrm{g}|\right) | \partial_{\varphi_j} \mathrm{g} \rangle = \frac{2\pi A^2}{\hbar^2} g_{jj},\end{aligned} \tag{SM20}$$

since $|\mathrm{g}\rangle \langle \mathrm{g}| + |\mathrm{e}\rangle \langle \mathrm{e}| = 1$.

Now, we proof Eq. 15 in the main text. The integrated rates read

$$\bar{R}_{jk}^{(\gamma)} = \frac{2\pi A^2}{\hbar^2 (2d)^2} \left| \langle \mathrm{e} | \left( \frac{\partial H_0}{\partial \varphi_j} + e^{i\gamma} \frac{\partial H_0}{\partial \varphi_k} \right) | \mathrm{g} \rangle \right|^2 \tag{SM21}$$

and, hence, the difference for two measurements with $\gamma_1 \neq \gamma_2$ yields

$$\begin{aligned}&\frac{\hbar^2}{2\pi A^2} \left( \bar{R}_{jk}^{(\gamma_1)} - \bar{R}_{jk}^{(\gamma_2)} \right) \\ &= \frac{1}{(2d)^2} \Bigg( \left| \langle \mathrm{e} | \left( \frac{\partial H_0}{\partial \varphi_j} + e^{i\gamma_1} \frac{\partial H_0}{\partial \varphi_k} \right) | \mathrm{g} \rangle \right|^2 \\ &\qquad - \left| \langle \mathrm{e} | \left( \frac{\partial H_0}{\partial \varphi_j} + e^{i\gamma_2} \frac{\partial H_0}{\partial \varphi_k} \right) | \mathrm{g} \rangle \right|^2 \Bigg) \\ &= \frac{1}{(2d)^2} \Bigg( \left[ e^{i\gamma_1} - e^{i\gamma_2} \right] \langle \mathrm{g} | \frac{\partial H_0}{\partial \varphi_j} | \mathrm{e} \rangle \langle \mathrm{e} | \frac{\partial H_0}{\partial \varphi_k} | \mathrm{g} \rangle \\ &\qquad + \left[ e^{-i\gamma_1} - e^{-i\gamma_2} \right] \langle \mathrm{g} | \frac{\partial H_0}{\partial \varphi_k} | \mathrm{e} \rangle \langle \mathrm{e} | \frac{\partial H_0}{\partial \varphi_j} | \mathrm{g} \rangle \Bigg) \\ &= \left[ e^{i\gamma_1} - e^{i\gamma_2} \right] \langle \partial_{\varphi_j} \mathrm{g} | \mathrm{e} \rangle \langle \mathrm{e} | \partial_{\varphi_k} \mathrm{g} \rangle \\ &\qquad + \left[ e^{-i\gamma_1} - e^{-i\gamma_2} \right] \langle \partial_{\varphi_k} \mathrm{g} | \mathrm{e} \rangle \langle \mathrm{e} | \partial_{\varphi_j} \mathrm{g} \rangle \\ &= \left[ e^{i\gamma_1} - e^{i\gamma_2} \right] \langle \partial_{\varphi_j} \mathrm{g} | (1 - |\mathrm{g}\rangle \langle \mathrm{g}|) | \partial_{\varphi_k} \mathrm{g} \rangle \\ &\qquad + \left[ e^{-i\gamma_1} - e^{-i\gamma_2} \right] \langle \partial_{\varphi_k} \mathrm{g} | (1 - |\mathrm{g}\rangle \langle \mathrm{g}|) | \partial_{\varphi_j} \mathrm{g} \rangle \\ &= \left[ e^{i\gamma_1} - e^{i\gamma_2} \right] \chi_{jk} + \left[ e^{-i\gamma_1} - e^{-i\gamma_2} \right] \chi_{jk}^{*}.\end{aligned} \tag{SM22}$$

For linear polarizations, i.e. $\gamma_1 = 0$ and $\gamma_2 = \pi$, we find Eq. 15a in the main text for $\mathrm{Re}(\chi_{jk}) = g_{jk}$. For circular polarizations, i.e. $\gamma_1 = \pi/2$ and $\gamma_2 = -\pi/2$, we find Eq. 15b in the main text for $\mathrm{Im}(\chi_{jk}) = -F_{jk}/2$.

## Section S5. 3-terminal junction: Hamiltonian, Weyl nodes and Chern number

In this section, we derive the effective low-energy Hamiltonian of a 3-terminal Josephson junction including a magnetic flux $\Phi = 3\alpha\Phi_0$ in the normal region, where $\Phi_0 = \hbar/2e$ is the flux quantum. The system is sketched in Figure S1A. Similar to the 4-terminal junction, the Hamiltonian for three terminals now reads

$$H = H_{\mathrm{D}} + \sum_{j=1}^{3} \left( H_{\mathrm{S}}^{(j)} + H_{\mathrm{S-D}}^{(j)} + H_{\mathrm{S-S}}^{(j,j+1)} \right), \tag{SM23}$$

with the Hamiltonians of the dot $H_{\mathrm{D}}$, the $j$-th superconducting lead $H_{\mathrm{S}}^{(j)}$ and the coupling between the $j$-th lead and the dot $H_{\mathrm{S-D}}^{(j)}$ as defined in the main text. The magnetic flux in the normal region modifies the direct hoppings between the leads only. Therefore, the coupling between the $j$-th and the $(j+1)$-th lead ($j = 3 \Rightarrow j+1 = 1$) is now given by

$$H_{\mathrm{S-S}}^{(j,j+1)} = t \sum\nolimits_{\boldsymbol{k}\sigma} \left[ e^{-i\alpha} c_{j\boldsymbol{k}\sigma}^{\dagger} c_{(j+1)\boldsymbol{k}\sigma} + \mathrm{H.c.} \right]. \tag{SM24}$$

Following the same steps as for the case of the 4-terminal junction, we obtain the effective low-energy Hamiltonian $H_0$, which again can be written as $H_0 = \boldsymbol{d} \cdot \boldsymbol{\tau}$, with

$$\boldsymbol{d} = \begin{pmatrix} \Gamma \sum_{j=1}^{3} \cos\varphi_j \\ -\Gamma \sum_{j=1}^{3} \sin\varphi_j \\ \varepsilon_0 - 2t_0 \Gamma \sum_{j=1}^{3} \cos(\alpha - \varphi_j + \varphi_{j+1}) \end{pmatrix}, \tag{SM25}$$

and the Andreev bound states $\varepsilon_{\mathrm{e/g}} = \pm d$, where $d = \sqrt{d_1^2 + d_2^2 + d_3^2}$. Gauge invariance allows us to set one SC phase to zero (we set $\varphi_3 = 0$ in the following). The spectrum is shown in Figures S1B-F for different values of $\alpha$. In this system, we find that Weyl nodes $\boldsymbol{\varphi}_{\mathrm{W}} = (\varphi_{\mathrm{W},1}, \varphi_{\mathrm{W},2}, \alpha_{\mathrm{W}})$, for which $d(\boldsymbol{\varphi}_{\mathrm{W}}) = 0$, only exist for $-6 \leq m \leq 6$ with $m = \varepsilon_0 / t_0 \Gamma$. There are four Weyl points located at (modulo $2\pi$ in each direction)

$$\boldsymbol{\varphi}_{\mathrm{W}}^{(1)} = \left(-2\pi/3,\, 2\pi/3,\, \alpha_{+}(m)\right), \tag{SM26a}$$

$$\boldsymbol{\varphi}_{\mathrm{W}}^{(2)} = \left(-2\pi/3,\, 2\pi/3,\, \alpha_{-}(m)\right), \tag{SM26b}$$

$$\boldsymbol{\varphi}_{\mathrm{W}}^{(3)} = \left(2\pi/3,\, -2\pi/3,\, -\alpha_{-}(m)\right), \tag{SM26c}$$

$$\boldsymbol{\varphi}_{\mathrm{W}}^{(4)} = \left(2\pi/3,\, -2\pi/3,\, -\alpha_{+}(m)\right), \tag{SM26d}$$

where

$$\alpha_{\pm}(m) = 2 \arctan\left( \frac{\sqrt{3} \pm 2\sqrt{1 - (m/6)^2}}{m/3 - 1} \right). \tag{SM27}$$

Each Weyl node $\boldsymbol{\varphi}_{\mathrm{W}}^{(s)}$, $s = 1, 2, 3, 4$, carries a topological charge $c_s$ which is obtained in the same way as for the 4-terminal junction. We find $c_{1,4} = \mathrm{sgn}(t_0)$ and $c_{2,3} = -\mathrm{sgn}(t_0)$. The locations and the charges of the Weyl points are shown in Figure S1G.

We define a first Brillouin zone (FBZ) as $(\varphi_1, \varphi_2, \alpha) \in [0, 2\pi)^3$ and calculate the Chern number $C$ as a function of $\alpha$ from the normalized effective field $\boldsymbol{n} = \boldsymbol{d}/d$ via

$$C(\alpha) = \frac{1}{4\pi} \int_0^{2\pi} \mathrm{d}\varphi_1 \int_0^{2\pi} \mathrm{d}\varphi_2 \left( \boldsymbol{n} \cdot \left[ (\partial_{\varphi_1} \boldsymbol{n}) \times (\partial_{\varphi_2} \boldsymbol{n}) \right] \right). \tag{SM28}$$

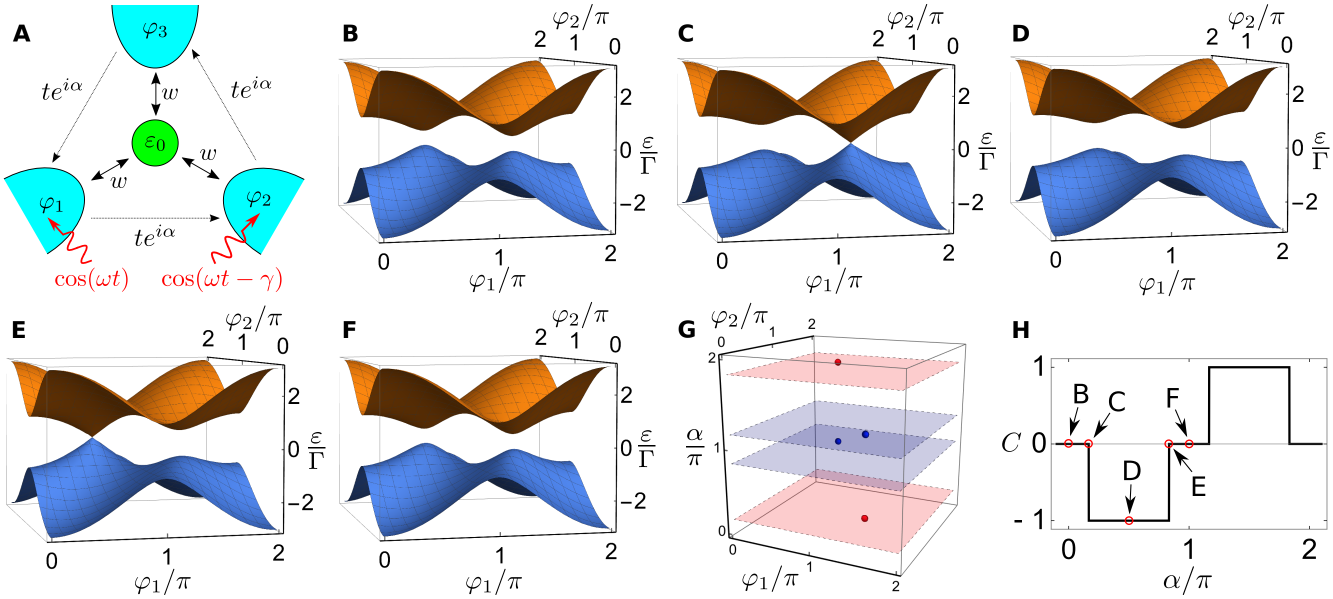

Figure S1. *Model, band structure, Weyl nodes and Chern number in a 3-terminal Josephson junction.* **(A)** Microscopic model of the 3-terminal junction. Three superconducting leads, each with a superconducting phase $\varphi_j$, are coupled to a normal dot with energy level $\varepsilon_0$ via the couplings $w$. The normal region is subjected a magnetic flux $\Phi = 3\alpha\Phi_0$ (flux quantum $\Phi_0 = \hbar/2e$) such that the couplings between the superconductors $t$ are modified by a phase factor $e^{i\alpha}$. Red wiggly arrows indicate that two up to two superconducting phases can be modulated at frequency $\omega$ and relative phase difference $\gamma$ to obtain information about the quantum geometric tensor. **(B-F)** Energy spectrum $\varepsilon_{\mathrm{e/g}} = \pm d$ for **(B)** $\alpha = 0$, **(C)** $\alpha = \pi/6$, **(D)** $\alpha = \pi/2$, **(E)** $\alpha = 5\pi/6$, **(F)** $\alpha = \pi$, respectively. **(G)** Locations of the four Weyl nodes in the FBZ. Blue (red) Weyl nodes carry a topological charge $c = +1$ ($c = -1$). The Chern number becomes nontrivial only if the $(\varphi_1, \varphi_2)$-plane of integration lies between two opposing charges. **(H)** Chern number $C$ as a function of $\alpha$. The points B, C, D, E and F correspond to the values of $\alpha$ in panels **(B)**, **(C)**, **(D)**, **(E)** and **(F)**, respectively. Common parameters for all panels: $t_0 = 0.1$, $\varepsilon_0/\Gamma = 0$.

The Chern number is shown in Figure S1H and shows topologically nontrivial regions for certain values of $\alpha$. Since we integrate over the phases $\varphi_1$ and $\varphi_2$, the finite jumps of $C$ are associated with the values $\alpha_\pm$ and $-\alpha_\pm$. In particular for $m = 0$, the four values of a topological phase transition are $\alpha_{\mathrm{W}} = \pi/6, 5\pi/6, 7\pi/6, 11\pi/6$ in the FBZ.